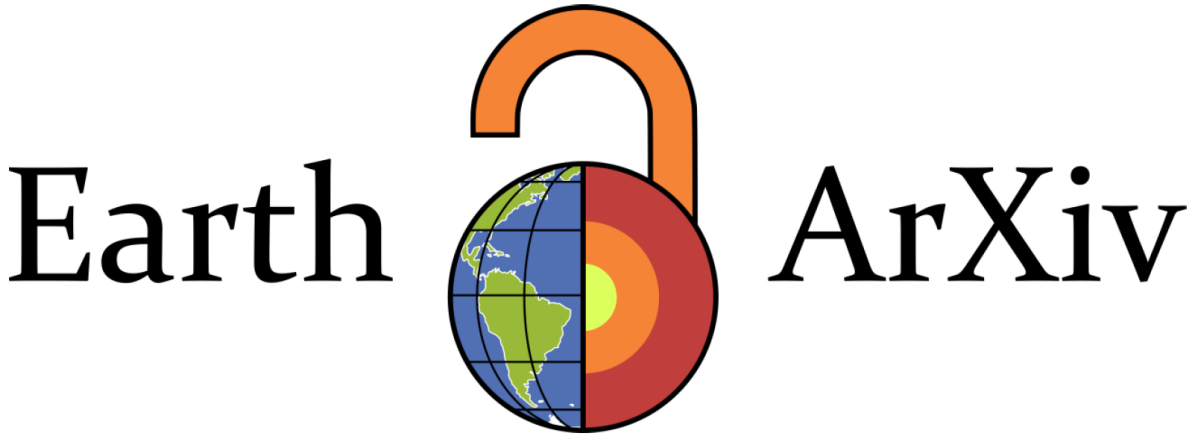

Simultaneous spectral induced polarization and X-ray µCT imaging to investigate pore-scale dynamics and geoelectrical responses in porous media

Hamdi Omar[1,2,3], Tom Bultreys[1,2], Flore Rembert[1,2], Sojwal Manoorkar[1,2], Frédéric Nguyen[3], David Caterina[3], and Thomas Hermans[1]

[1] Department of Geology, Ghent University, Belgium

[2] Centre for X-ray Tomography (UGCT), Ghent University, Belgium

[3] Urban and Environmental Engineering, Liege University, Liege, Belgium

SUMMARY:

Understanding the interplay between pore-scale fluid distribution and bulk electrical properties is critical to improving petrophysical models of partially saturated porous media. This study introduces and evaluates a novel experimental setup that enables synchronized spectral induced polarization (SIP) and X-ray micro-computed tomography (µCT) measurements under dynamic saturation conditions. A custom-designed flow cell was developed to accommodate both high-resolution µCT imaging and accurate SIP acquisition at the same time. It includes retracted, non-polarizable potential electrodes placed in agar-filled channels, which minimize electrode polarization and preserve signal integrity during measurement. Using this setup, we conducted a drainage–imbibition experiment on an unconsolidated sand sample. High-resolution µCT images captured the evolving spatial distribution of the water phase, while simultaneous SIP data provided complementary information on bulk resistivity and phase connectivity. We extracted the fluid distribution in the pore network from segmented images and computed both geometric and electrical tortuosity to investigate how pore-scale and transport parameters are related. A pore network model (PNM), extracted from the dry µCT scan, was used to simulate resistivity index (*RI*) trends, allowing for direct comparison between experimental and modelled values. Results show that saturation history significantly impacts both resistivity and tortuosity, with notable differences between drainage and imbibition. The µCT data confirm that trapped gas phases and connectivity losses are key drivers of marked resistivity increases. While the tested sample exhibited limited polarization, the experimental platform proved effective in linking microstructure to geoelectrical response. The combined SIP–µCT method offers a promising route for refining petrophysical models and holds potential for future studies involving more complex, polarization-prone materials and biogeochemical processes.

1. INTRODUCTION

Geophysical methods have become indispensable tools for characterizing and monitoring subsurface processes across a wide range of applications, including hydrogeology, environmental remediation, and reservoir engineering. (e.g., Berkowitz & Scher 1998; Allen & Allen 2013; Revil & Florsch 2010; Wildenschild & Sheppard 2013). In particular, electrical and electromagnetic methods enable time-lapse monitoring of fluid movement, contaminant transport, and reactive processes, offering non-invasive access to dynamic subsurface changes (Hermans et al. 2023; Singha et al. 2015). Electrical conductivity and spectral induced polarization (SIP) are increasingly used for high-resolution spatial and temporal monitoring of hydrological processes both at the field and laboratory scale (Hermans et al. 2023; Dimech et al. 2022; Slater & Binley 2021). SIP is a geophysical technique that measures the frequency-dependent complex electrical conductivity of geomaterials, which is sensitive to ionic mobility, fluid content, and surface conductivity (Revil & Florsch 2010; Schmutz et al. 2010). Pore-scale dynamics affect bulk electrical conductivity as well as interfacial polarization mechanisms at various frequencies, which can both be measured using SIP method (Wildenschild & Sheppard 2013; Jougnot et al. 2010).

Despite its growing application, quantitative interpretation of geoelectrical data remains a major challenge. This limitation stems largely from the complexity of subsurface environments and a limited understanding of the petrophysical relationships that link the geophysical response to hydrological and geochemical properties. Indeed, while pore-scale processes such as drainage, imbibition, mineral dissolution, and biofilm growth shape electrical signals by modifying the structure and connectivity of the fluid pathways, the electrical response due to different processes and heterogeneity is non-trivially coupled in practice. As a result, electrical imaging remains often interpreted qualitatively due to uncertainties on how the spatial

distribution of fluid saturation, pore connectivity, and surface chemistry influence electrical properties such as resistivity and induced polarization (Revil & Florsch 2010; Binley & Kemna 2005). Despite significant research efforts, it has proven challenging to disentangle geoelectrical responses, partly because traditional experimental approaches (such as column flow tests and saturated/unsaturated core-scale measurements) provide bulk responses that average over multiple coupled processes, making it difficult to resolve distinct contributions from phenomena like mineral precipitation, wettability changes, or biofilm growth (Binley & Kemna 2005; Revil & Florsch 2010).

A potential solution to approach this issue is to combine pore-scale imaging with geoelectrical measurements. Simultaneous measurements combining SIP and imaging techniques have been explored in recent studies but have so far been limited to 2D microscopy approaches. For example, Rembert et al. (2023a) successfully coupled real-time SIP measurement with high-resolution optical microscopy to monitor the dynamics of calcite dissolution in a microfluidic chip, enabling direct correlation between interfacial geochemical reactions and electrical signatures. Nonetheless, such 2D systems are inherently limited in capturing the full three-dimensional pore geometry and fluid distribution, which are critical for interpreting subsurface processes. X-ray micro-computed tomography (µCT), on the other hand, provides micrometer-scale visualization of pore network in 3D, enabling quantitative analysis of geometry, connectivity, and tortuosity (Bultreys, 2016; Wildenschild and Sheppard 2013). While sequential use of SIP and µCT has advanced our understanding of how pore-scale features influence geophysical responses (Adebayo et al. 2017; Atekwana and Slater 2009; Bauer et al. 2011; Cimpoiaşu et al. 2021; Hao et al. 2021; Johansson et al. 2019; Ma et al. 2025; Rembert, et al. 2023; Revil, et al. 2014; Yan et al. 2018; Zhang et al. 2018; Izumoto et al. 2022), simultaneous measurements that ensure both modalities capture the same sample state remain rare, particularly under controlled multi-phase conditions. One notable exception is the work

by Zhao et al. (2022), who developed an experimental setup that enables simultaneous µCT imaging and resistivity measurements. Their setup, however, recorded only the real (resistive) component of electrical conductivity, without capturing the imaginary (capacitive) component that is essential for comprehensive characterization of pore-scale electrochemical and interfacial processes.

To date, no study has implemented a fully synchronized SIP and 3D imaging framework, such as µCT, leaving a gap in our ability to directly observe and quantify the dynamic interplay between pore structure and electrical properties in three dimensions. In many systems, dynamic processes cannot be paused or interrupted without altering them, which makes stop-and-go or sequential measurements impractical. Moreover, in cases where such interruptions are possible, the timescales of structural changes, such as those driven by mineral precipitation, dissolution, microbial activity, or redox cycling, are often too short relative to the interval between imaging and SIP acquisition. These processes can modify pore morphology, block or open flow paths, and change interfacial areas, all of which directly influence SIP signals (Tokunaga, 2009; Weller et al. 2015; Leroy et al. 2008; Slater et al. 2006; Zhang et al., 2021). Without synchronized imaging, these effects may be misinterpreted or entirely overlooked. For instance, SIP phase shifts observed during acid-induced carbonate dissolution might be attributed solely to increased porosity, while simultaneous imaging would reveal that changes in surface roughness or bubble formation also contribute significantly to the signal (Schwartz et al. 2014).

To address these limitations, we introduce a novel experimental setup that enables simultaneous SIP and µCT acquisition, capturing the co-evolution of geoelectrical signals and 3D pore-scale structure and fluid distribution during multiphase flow experiments. Our setup includes a custom-built flow cell that allows direct monitoring of air-water displacement in a sand pack under drainage and imbibition cycles. This approach provides several advantages:

(1) Time-resolved dynamic monitoring: it captures transient processes, such as fluid redistribution, with direct spatial and electrical correspondence.

(2) Enhanced interpretability: it enables direct correlation of SIP signatures with visual evidence of pore-scale mechanisms such as capillary trapping or phase invasion.

(3) Improved model validation: it supports quantitative comparison between observed SIP responses and image-based pore network simulations, helping to bridge the gap between experimental data and digital rock physics.

In this study, we present a novel experimental setup that enables simultaneous SIP and 3D X-ray μCT imaging. We apply this setup to a controlled drainage–imbibition experiment in a saturated sand pack to investigate the co-evolution of fluid distribution and electrical response. To validate the approach, we calculated the resistivity index (*RI*) and tortuosity from both SIP data and μCT-derived pore network models. We compared the results to assess where the methods agree or diverge, and how μCT data help explain variations in electrical behaviour. This methodology aims to contribute to the development of more accurate petrophysical models based on pore-scale processes and observations, with implications for subsurface resource management, contaminant transport, and carbon storage.

2. MATERIALS AND METHODS

2.1. Experimental Setup and Sample Holder Description

This study presents a novel set-up that allows to combine simultaneous SIP and 3D μCT monitoring, compared to past sequential measurement protocols (Johansson et al. 2019). The system includes a Hassler-type core holder, designed for flow experiments under well controlled pressure and temperature (**Fig. 1**, see supplementary information for further details). The core holder is composed of a high-grade aluminium flow-cell, which contains the sample holder in a confining liquid (**Fig. 1**a). The aluminum tube, with a wall thickness of 3 mm,

balances mechanical strength with sufficient X-ray transparency to allow µCT scanning. An isostatic confining pressure is applied using non-conductive oil, which uniformly compresses a cylindrical rubber sleeve containing the sand sample. A four-electrode system is coupled to the core holder to allow SIP measurements, considering several design factors to collect accurate signals (e.g., Zimmermann et al. 2008). First, to maintain electric field homogeneity across the electrodes for electric current injection, the sample width-to-length ratio should not exceed 1:2. The sample holder comprises a 12 cm cylindrical rubber sleeve with an inner diameter (ID) of 15.2 mm and an outer diameter (OD) of 17.2 mm, thus, not exceeding a 1:6 width-to-length ratio. Second, it is recommended to maintain a potential-current electrode separation of at least twice the sample width. A four-electrode array in the Wenner-α configuration (e.g., Binley and Kemna, 2005) with 30 mm spacing between the electrodes is used. This configuration minimizes polarization effects and enables impedance measurements across a broad frequency spectrum. The current injection electrodes are in titanium, a non-polarizable material that minimizes interfacial polarization effects when in contact with the geomaterial. These electrodes feature dual-channel functionality, serving both as electrical current injectors and as fluid/gas injection ports. Each current electrode has a cylindrical shape with a diameter of 15.2 mm and a height of 25 mm, out of which 15 mm are inserted inside the rubber sleeve (**Table 1**). The electrodes are inserted from both ends of the sample holder (**Fig. S1** in supporting information), ensuring homogeneous contact with the sample and enabling uniform current injection across the entire sample volume.

A key feature of the experimental setup was to design retracted non-polarizable electrodes for accurate electrical potential measurement. Potential electrodes made of metallic materials are prone to polarization effects. When these electrodes are positioned directly within the sample, they can become polarized due to the injected current, even when the voltage difference across them is minimal (e.g., Zimmermann et al. 2008). To minimize this unwanted

polarization, it is recommended to retract the potential electrodes outside the sample whenever feasible (e.g., Zimmermann and Huisman, 2024). Our configuration builds on this concept with a practical, integrated design: each potential electrode consists of a hollow PEEK (polyether ether ketone) screw (outer diameter 4 mm, inner diameter 2 mm) filled with KCl-agar gel, which maintains ionic contact with the sample (**Fig. S1**). This screw is inserted through the rubber sleeve wall and tightly sealed using a brass nut that also acts as the conductive contact. The brass nut is soldered to a stainless-steel wire, which passes through the confining liquid (non-conductive oil) and connects to the SIP measurement system (see supplementary text S1 for more technical details). This setup ensures stable potential measurements, minimizes polarization effect, and preserves a seal against the confining pressure.

Table 1. Characteristics and sizing of the sample holder

Sample holder components	**Shape and Material**	**Cylindrical rubber sleeve**
	Height (mm)	120
	Inside diameter-ID (mm)	15.2
	Outside diameter-OD (mm)	17.2
	Thickness (mm)	2
Injection electrodes	Material	Titanium
	Height (mm)	20
	Diameter (mm)	15.4
Potential electrodes	Material	Brass nut
		Extruded PEEK screws filled with KCl-agar gel

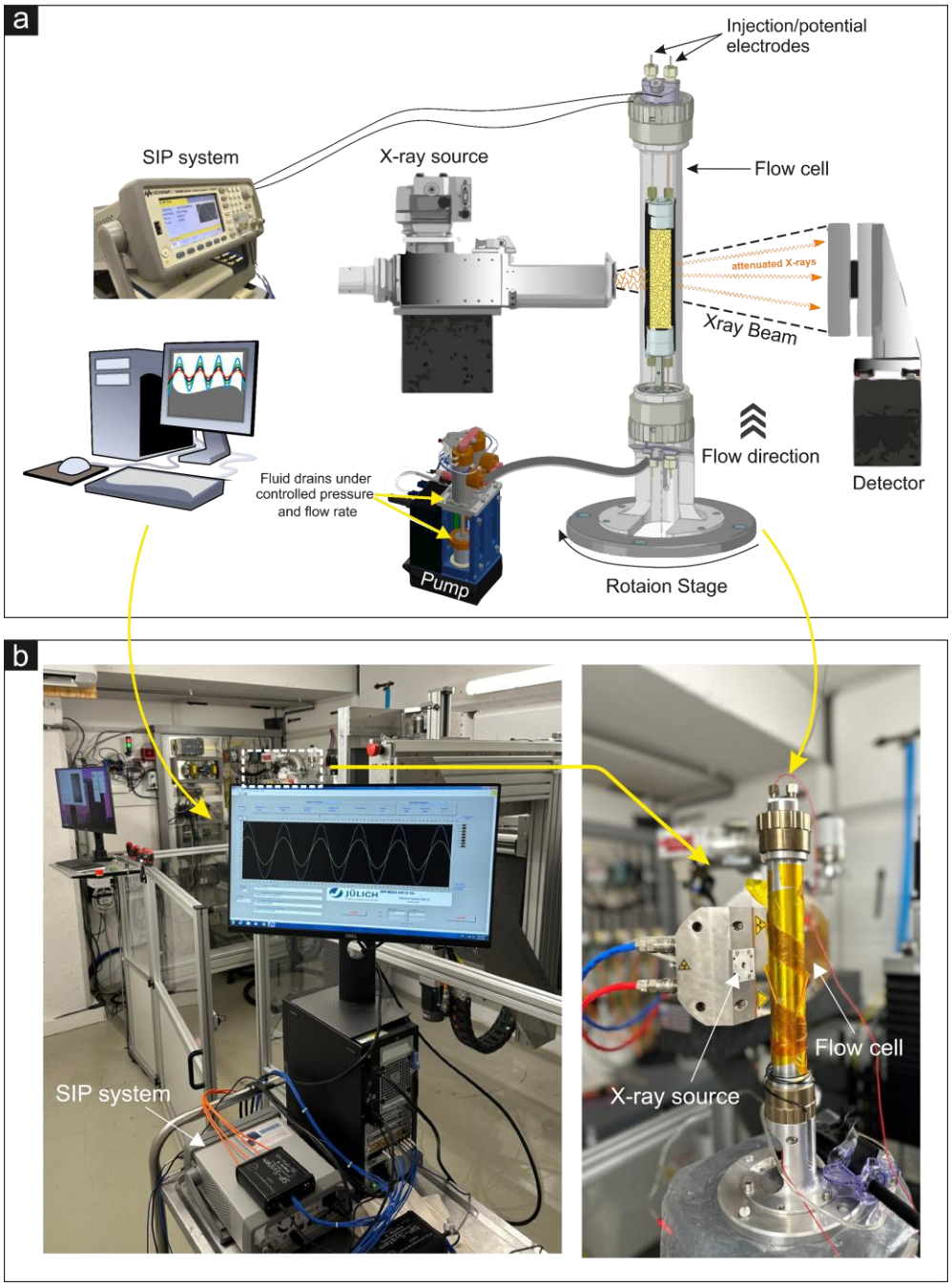

Figure 1. General overview of the laboratory setup developed for this study. (**a**) Schematic diagram of the experimental setup. (**b**) Photograph of the setup showing the SIP system connected to the flow-cell, which is mounted on the rotation stage in front of the X-ray source. (**c**) Close-up view of the flow-cell, within which the sample holder (described in **Fig. S1**) is installed. A manual syringe filled with non-conductive oil is fixed on the rotation stage to maintain a constant confining pressure of at least 25 bars throughout the experiments.

2.2. Experimental protocol for combined SIP and µCT analysis

This study presents the results of the first synchronized SIP and µCT experiment obtained with the newly developed setup, designed to evaluate its performance and demonstrate its added value. A single drainage–imbibition experiment was carried out on a cylindrical column of unconsolidated, fine-grained sand, saturated with a 0.1 S m^{-1} NaCl solution. The objective was to monitor the coupled evolution of fluid distribution and electrical response across a range of saturation states. Drainage was induced by stepwise nitrogen gas injection under increasing pressures, while imbibition was driven by staged water reinjection at controlled flow rates. During the experiment, a total of seven combined SIP and µCT datasets were collected. The procedure included the following steps:

1. Initial dry state (S0): X-ray scan of the dry, unconsolidated fine-grained sand packed in the sample holder.
2. Full saturation (S1): Full saturation of the sample with a 0.1 S m^{-1} sodium chloride (NaCl) solution.
3. Drainage step 1 (S2): Injection of nitrogen gas at 1 bar pressure for 20 minutes to initiate drainage.
4. Drainage step 2 (S3): Increased gas injection pressure to 5 bar for 20 minutes.
5. Drainage step 3 (S4): Further increase to 10 bar for 20 minutes.
6. Imbibition step 1 (S5): Re-injection of 15 ml NaCl solution at 2 ml per minute.
7. Imbibition step 2 (S6): Additional 15 ml injected at 5 ml per minute.
8. Full re-saturation (S7): Final injection of 10 ml at 10 ml per minute to reach full water saturation again.

For all experiments, direct SIP measurements and µCT images were acquired in synchronized steps. Each SIP spectrum was recorded over approximately 20 minutes, while the

X-ray µCT projections began 1–2 minutes after the start of the SIP measurement, with both acquisitions running in parallel. The µCT scan lasted about 35 minutes, so that the SIP measurement time entirely overlapped with the µCT acquisition. This stepwise protocol enabled the monitoring of electrical and water content changes throughout the drainage and imbibition cycle under controlled and reproducible conditions.

2.3. SIP acquisition and sample holder validation

The complex electrical resistivity of the sample was acquired using the SIP system developed by Zimmermann et al. (2008). A sinusoidal current $I(\omega)$ with a frequency f ranging from 10 mHz to 45 kHz was injected between the current electrodes. The resulting electric voltage $U(\omega)$ was measured between the potential electrodes (P1 and P2 in **Fig. S1**c). The input current follows a sinusoidal waveform expressed as,

$$I(t) = |I|\, sin(\omega t) \quad (1)$$

where |I| is the current amplitude (A), and ω=2πf (rad/s) is the angular frequency. The measured voltage has a similar sinusoidal form but is typically shifted in phase,

$$U(t) = |U|\, sin(\omega t + \varphi) \quad (2)$$

with $|U|$ being the voltage amplitude (V) and φ is the phase shift between current and voltage. For analytical convenience, both current and voltage are represented in complex notation,

$$I^* = |I|e^{i\varphi},\ U^* = |U|e^{i\varphi} \quad (3)$$

The complex electric impedance Z(ω) which reflects the combined resistive and capacitive behaviour of the sample, is derived from the ratio of the injected current and the measured voltage,

$$Z^* = \frac{U^*}{I^*} = |Z(\omega)|e^{i\varphi} \quad (4)$$

where, |Z(ω)| is the amplitude, and i is the imaginary unit ($i = \sqrt{-1}$). The measured

electrical impedance is influenced by the sample geometry and electrode configuration (Zimmermann et al. 2008). To consider this, a geometrical factor k_G (m) is introduced. It relates the measured impedance to the bulk electrical conductivity σ (S m^{-1}) of the medium, an intrinsic property. The geometrical coefficient k_G was determined experimentally by measuring the complex impedance of the sample holder filled with NaCl solutions between 10 mHz and 45 kHz at five different conductivities σ_w ranging between 4×10^{-3} and 3×10^{-2} S m^{-1} (see the results in **Fig. S2**). For each conductivity, we calculated $k_G = 1/(|Z(\omega)|\sigma_w)$ at the lowest frequency (f = 10 mHz). This is because all subsequent resistivity modelling, including Archie's law and its derivatives, is based on DC current, which most closely corresponds to the lowest frequency used in this study. The use of several solutions enables establishing a linear relationship between $|Z(\omega)|$ and σ_w, where k_G is the inverse of the slope of the linear regression (**Table S2**). This approach ensures a geometry-specific calculation of k_G, independent of the water conductivity, by minimizing systematic errors and validating the linearity of the data. Thus, we determined $k_G = 0.0683 \pm 0.0011$ m (**Fig. S2**).

The measurements on water samples show that the phase angle shifted systematically with increased water conductivity to a maximum of 3.5 mrad in the 10 mHz – 1 Hz frequency range. These values, obtained across a wide range of fluid conductivities, exceed the ±0.3 mrad reported by Lesmes and Frye (2001) (at 0.0085 S m^{-1}) using a similar setup and frequency range. Our uncertainty is also greater than the ±0.1 mrad achieved by Zimmermann et al (2008) with a setup optimized for low-phase-angle investigations. The consistent phase offset suggests that the effect arises from electrode-fluid interface polarization. This is supported by the fact that the reciprocal measurements do not show any phase shift, further pointing to electrode asymmetry as a likely source for this shift (**Fig. S2**d). However, considering the minor polarization observed during the sample holder

validation (1–3.5 mrad, **Fig. S2**b), the reproducibility of measurements over time and the consistent trends observed across water with different conductivities (**Fig. S2**b), suggest that these effects do not significantly impact the interpretation of saturation-dependent trends in our experiment (Zimmermann and Huisman 2024).

2.4. Theoretical background: Archie's exponents and tortuosity

2.4.1. Archie's law

Rock conductivity is strongly governed by how water and other conductive fluids are arranged within the pore network, which is often intricate and heterogeneous (Norbisrath et al. 2015). To describe this behaviour, empirical frameworks such as Archie's law and its generalizations (Glover et al. 2000; Glover 2009; Glover, 2010; Glover 2017) have become standard tools in geophysical applications (e.g., Niu & Zhang 2018, Cong-Thi et al. 2024). One key parameter derived from these models is the dimensionless resistivity index, which links electrical resistivity to fluid saturation through the saturation exponent n. It reflects how the connectivity and the spatial distribution of the conductive aqueous phase impact the evolution of the electrical resistivity during drainage and imbibition (Archie, 1942; Glover, 2009; Glover, 2017). Glover (2015) also offers a comprehensive theoretical treatment of n, emphasizing its dependence on the spatial arrangement of wetting and non-wetting fluids, a distribution shaped by pore geometry, capillarity, connectivity, and wettability. In this study, we derive n from log-log fitting of the resistivity index (RI) versus water saturationError! Reference source not found., based on Archie's second law (Archie, 1942). Archie's first law defines the formation factor F under saturated conditions as:

$$F = \frac{\rho_0}{\rho_f} = \phi^{-m} \quad (5)$$

where ρ_0 is the resistivity of the fully saturated porous medium, ρ_f the resistivity of the saturating aqueous solution, ϕ is the porosity of the rock, and m is the cementation exponent (Glover, 2009), and the ratio F called formation resistivity factor (corresponding values of Archie's parameters are provided in **Table 2**). Given measurements of ρ_0, ρ_f , and ϕ, the exponent m can be calculated by rearranging Eq. (5) as,

$$m = -\frac{log\, F}{log\, \phi} \quad (6)$$

This empirical parameter is broadly used because it is found constant for a rock type and it typically ranges between 1.5 and 5 (e.g., Glover, 2015). Its value increases as the degree of connectivity of the pore network diminishes. In our experiment, we obtained a cementation exponent of m = 1.67, which falls closer to the lower end of the expected range for sand (Glover, 2016). For partially saturated conditions, Archie's second law introduces the resistivity index,

$$RI = \frac{\rho_b}{\rho_0} = S_w^{-n} \quad (7)$$

where ρ_b is the bulk resistivity of the rock at saturation S_w, and RI is the ratio of unsaturated to saturated resistivity and n is the saturation exponent. The saturation exponent can be determined empirically by taking the logarithm of Eq. (7), which gives the linearized form used for fitting n,

$$log(RI) = -n\, log(S_w) \quad (8)$$

The electrical conductivity of a porous rock, particularly when partially saturated with an aqueous phase, is highly sensitive to variations of this parameter (Glover, 2017).

2.4.2. Tortuosity

Despite its long-standing use in porous media research, the concept of tortuosity remains ambiguously defined and inconsistently applied (Fu et al. 2021). While the term intuitively refers to the complexity of transport pathways, a wide variety of models and definitions have been proposed over the decades, often with limited coherence between them. As noted by multiple authors (e.g., Tye, 1983; Epstein, 1989; Sahimi, 1993; Moldrup et al. 2001), the literature on tortuosity can be misleading, particularly when different definitions are treated interchangeably. No unified framework has yet emerged that reconciles geometric, hydraulic, electrical, and diffusive formulations in a consistent way (Fu et al. 2021; Ghanbarian et al. 2013). Tortuosity may be defined as a purely geometric parameter, such as the ratio of average path length to straight-line distance, or as a transport-specific factor related to effective hydraulic conductivity, or diffusivity (Scheidegger, 1974; Clennell, 1997; Matyka et al. 2008). These process-based definitions inherently embed not only the geometry of the pore space but also the physics of the transport mechanism under study. As such, tortuosity is now widely acknowledged to be a process-dependent property rather than an intrinsic material constant (Ghanbarian et al. 2013; Fu et al. 2021).

In this study, we focus on two specific measures of tortuosity: geometric tortuosity, derived from segmented μCT images, and electrical tortuosity, calculated from SIP-derived conductivity data as a function of water content. We aim to explore the correspondence (and divergence) between structure-based and transport-based tortuosity measures, by evaluating these two metrics across a series of controlled saturation steps. This comparison illustrates the added value of combining SIP with μCT imaging for pore-scale characterization. In particular, it allows to assess the sensitivity of electrical and geometric tortuosity to changes in phase connectivity, and to evaluate the extent to which image-derived metrics capture the dynamic nature of geoelectrical properties under partial saturation.

Geometrical tortuosity is recognized as a fundamental microstructural attribute, entirely dictated by the spatial arrangement and morphology of the pore network within a porous medium (Clennell, 1997). It is generally defined as the following ratio,

$$\tau_g = \frac{\langle L_g \rangle}{L_s} \quad (9)$$

where $<L_g>$ is the average length of the geometric flow paths through the medium and Ls is the straight-line length, L_s, across the medium (Ghanbarian et al. 2013). Geometric tortuosity was estimated from segmented μCT images using the open-source software *TauFactor 2* (Kench et al. 2023). This is a GPU-accelerated Python tool that computes, in complex 3D geometries, the tortuosity factor based on effective transport simulations through voxelized microstructures. The output tortuosity factor reflects the relative lengthening of transport paths induced by pore morphology, and is used here as a proxy for geometric tortuosity in both fully and partially saturated media.

To complement the structure-based analysis, electrical tortuosity was calculated based on the expression (Wyllie, 1957; Schopper, 1966; Dullien, 1979; Clenell, 1997; Coleman & Vassilicos 2008; Glover, 2015),

$$\tau_e = F\phi \quad (10)$$

where F is the formation factor and ϕ is the porosity. In saturated conditions, Archie's law relates the formation factor to porosity through the cementation exponent m (Eq. 5), while in partially saturated porous media eq. (5) becomes,

$$F = \phi^{-m} S_w^{-n} \quad (11)$$

Furthermore, in partially saturated conditions, porosity must be adjusted to account for the actual volume of conductive fluid present. This is done by replacing total porosity ϕ with water content θ:

$$\theta = S_w \, \phi \quad (12)$$

This adjustment reflects the fact that non-conductive phases such as air behave similarly to solid grains in terms of electrical conduction, effectively reducing the conductive pore volume. As a result, the expression for effective electric tortuosity becomes dependent on both porosity and saturation, and is given by:

$$\tau_{e,eff} = \phi^{1-m} \; S_w^{1-n} \quad (13)$$

where ϕ is porosity (0.32), and S_w is the water saturation.

2.5. X-ray µCT imaging and image analysis

X-ray imaging was conducted using the 'High Energy micro-CT Optimized for Research' (HECTOR) scanner at the Ghent University Center for X-ray Tomography (UGCT). The scans were performed at an X-ray energy of 150 kV and a power of 15 W. A total of 2001 projections were acquired, each with an exposure time of 1000 ms. The region of interest (ROI) was scanned at each saturation step, with a field of view (FOV) of 2400 × 2400 × 1400 voxels and a voxel size of 17.24 µm. The 3D reconstruction of the acquired projections was carried out using Octopus software (Tescan-XRE, Belgium). Post-processing of the reconstructed images was performed using Avizo (ThermoFisher Scientific) software, where all partially saturated and re-saturated sample scans were registered to the dry scan using normalized mutual information. Noise reduction was applied using a non-local mean filter with a similarity value of 0.4. The pores and grains in the dry scan were segmented through global thresholding and subsequently used as a mask to segment air and water in the scans with different saturation conditions. Basic image analysis allows for the extraction of key physical characteristics of the sample: the total porosity was estimated from the segmented dry scan, while fluid saturations

were determined based on volume fractions of the segmented phases. In this case, the computed 3D porosity falls within the 32–33% range, values that are typical for materials composed of loosely arranged, unconsolidated grains (Aggelopoulos et al. 2005; Garba et al. 2019).

The dry scan provides a high-resolution representation of the pore structure, which serves as the geometric basis for further analysis. Although this scan does not capture the evolving fluid distribution during the drainage–imbibition cycle, it allows construction of a static pore network that can be used to simulate multiphase behaviour. One of the goals of this study is to show that the proposed method enables a meaningful comparison between simulated and observed *RI* trends. This comparison aims to evaluate pore network-based simulations (*RI* in this case) to bridge the gap between empirical geoelectrical laws and physically-based pore structure characteristics. We extracted the pore network from the segmented μCT image of the dry sample using the *PNExtract* pore network extraction code (Raeini et al. (2018). The method provides a simplified but topologically representative structure of the pore space which can be used for two-phase flow simulations. Next, we employed *PNFlow*, an open-source pore-network simulation tool developed by Raeini et al. (2018), to model the evolution of the *RI* from dry-scan-derived pore network. *PNFlow* computes two-phase fluid distributions through a quasi-static invasion-percolation algorithm, which assumes fully capillary-dominated flow. This approach determines the spatial distribution of wetting and non-wetting phases for a given saturation level. We first simulated a drainage process starting from full saturation down to a minimum water saturation of S_w = 0.1, followed by an imbibition sequence to re-establish higher saturations. Once the fluid configuration is defined, *PNFlow* applies conservation of charge to solve for electrical transport through the network. Electrical conductance values are assigned to each pore and throat based on simplified geometries and local fluid occupancy, assuming electrolytic conduction as the sole transport mechanism and neglecting surface conductivity. The model simulates resistivity at different saturation states, up to a maximum S_w

of 0.84. The resulting *RI* values were compared with those derived from experimental SIP measurements during the drainage and imbibition cyclesError! Reference source not found..

The water phase filling the pores acts as the principal conductive medium in the analysed sample, and its distribution plays a central role in determining the relationship between resistivity and pore water saturation. To quantify water occupancy in the pore space, we compared the segmented water-phase μCT images (S1 – S6) against the single dry-state μCT image of the sand sample. The segmented dry image was processed using *PNExtract*, which assigns a unique pore label to each voxel within the pore space according to its association with a pore in the extracted pore network model. Each labelled pore was then cross-referenced voxel-wise with the corresponding water-phase image, where voxels representing water were assigned a value of 1 and 0 for anything else. A pore was classified as "water-filled" if more than 50% of its voxels were identified as water in the segmented image. This comparison was repeated for each saturation step, resulting in a list of water-filled pores per image. Using these, we extracted and compared the distributions of network properties (pore size, volume, throat size, connectivity) between the dry pore space and the water-occupied pore space at each stepError! Reference source not found..

3. RESULTS AND DISCUSSION

3.1. Analysis of resistivity and saturation-dependent changes

Error! Reference source not found.**Figs. 2** and **3** present the evolution of SIP responses across different saturation states, showing clear saturation-dependent trends in impedance behaviour during both drainage (S1–S3) and imbibition (S4–S6)**Error! Reference source not found.**. The magnitude of resistivity $|\rho|$ increases as the sample transitions from full to partial saturation (**Fig. 2**d), due to the replacement of conductive water by non-conductive gas phase,

which reduces the electrical connectivity through the sample (Revil & Florsch 2010; Weller et al. 2015). During re-saturation, the resistivity decreases, yet a persistent offset suggests the presence of residual gas trapping and incomplete water reconnection in the pores, consistent with previous observations of hysteresis effects in geoelectric properties (Binley et al. 2002). The resistivity spectra are flat (**Fig. 2**a), showing no frequency dependence, as expected for a clean sand sample.

The phase φ reaches low values close to zero due to the clean sand sample investigated. Nevertheless, φ exhibits slight decrease (more negative values) and increase (negative values closer to zero) during drainage (**Fig. 2**d) that could indicating enhanced interfacial polarization effects at gas–brine interface (Leroy et al. 2008; Schmutz et al. 2010; Zhang et al. 2021). Some electromagnetic noise is affecting the phase spectra for frequencies above 500 Hz. The real component of the complex resistivity ρ' follows a similar trend than the magnitude of the complex resistivity (**Fig. 2**c). It increases during drainage and remaining elevated post re-saturation due to disconnected conductive pathways caused by trapped gas (Slater & Binley 2021; Weller et al. 2011). The imaginary component (ρ'') shows broad peaks at lower frequencies (typically below 10 Hz) under partially saturated conditions (**Figure 2**d), especially during late drainage (S2 – S3), with signal intensity diminishing in more saturated conditions (S4 – S6). These peaks become less pronounced during imbibition which could be attributed to electrode and membrane polarization effects. These observations confirm that SIP responses are highly sensitive to saturation history, with clear hysteresis effects between drainage and re-saturation, aligning with findings from experimental and modelling studies on dynamic fluid distribution and resistivity (Doussan & Ruy 2009; Rembert et al. 2023b).

The µCT images provide a detailed visualization of fluid redistribution across the different saturation states (Error! Reference source not found.a and b), to investigate the complex interactions between pore network and fluid connectivity. During drainage (S1–S3), the

injection of nitrogen gas progressively displaces the conductive water, leading to the formation of (seemingly) disconnected water ganglia within pore throats and larger gas-filled voids in the centre of large pores (Error! Reference source not found.a). While the images suggest localized water entrapment, these features likely correspond to water films or corner layers that remain connected but fall below the µCT resolution. Such sub-resolution pathways maintain hydraulic continuity, although with significantly reduced conductivity compared to fully saturated pores. This saturation pattern is consistent with previous findings that gas preferentially invades larger, well-connected pores, while finer pores retain water due to capillary trapping (Armstrong et al. 2012; Tokunaga 2009; Wildenschild & Sheppard 2013). The observed gas percolation pathway confirms that drainage is strongly controlled by pore throat size and connectivity, in agreement with previous studies on multiphase flow in porous media (e.g., Berg et al. 2013). Upon re-saturation (S4 – S6), fluid reinjection gradually restores water connectivity, but complete reconnection is hindered by residual trapped gas (Pentland et al. 2011). These gas pockets reduce effective water saturation and bulk conductivity, while the constrained geometry of water films enhances interfacial polarization. These effects are reflected in the SIP measurements (**Figs 2Figure *2*** and **3Figure *3***), which show decreased conductivity and moderate increases in phase shift under partial saturation (Revil et al. 2011).

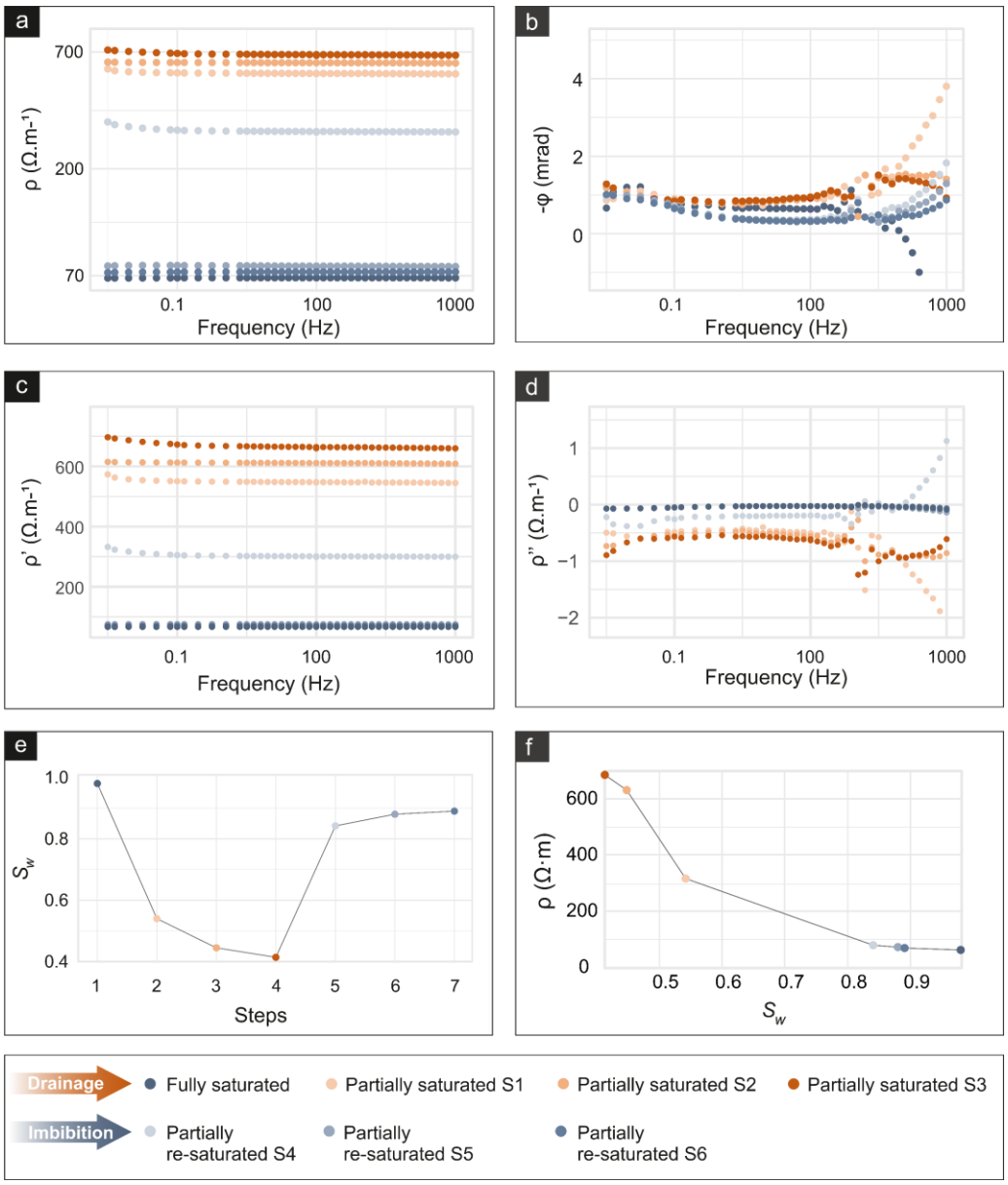

Figure 2. Electrical and saturation properties of the sample at varying water saturation states. (**a**) Resistivity (ρ) as a function of frequency. (**b**) Phase of complex impedance versus frequency. (**c**) Evolution of water saturation (S_w) during drainage and imbibition steps. Sample labels (S1–S6) correspond to specific saturation states, including fully saturated, partially saturated, and partially re-saturated conditions. (**d**) Resistivity versus water saturation (at 10 mHz frequency).

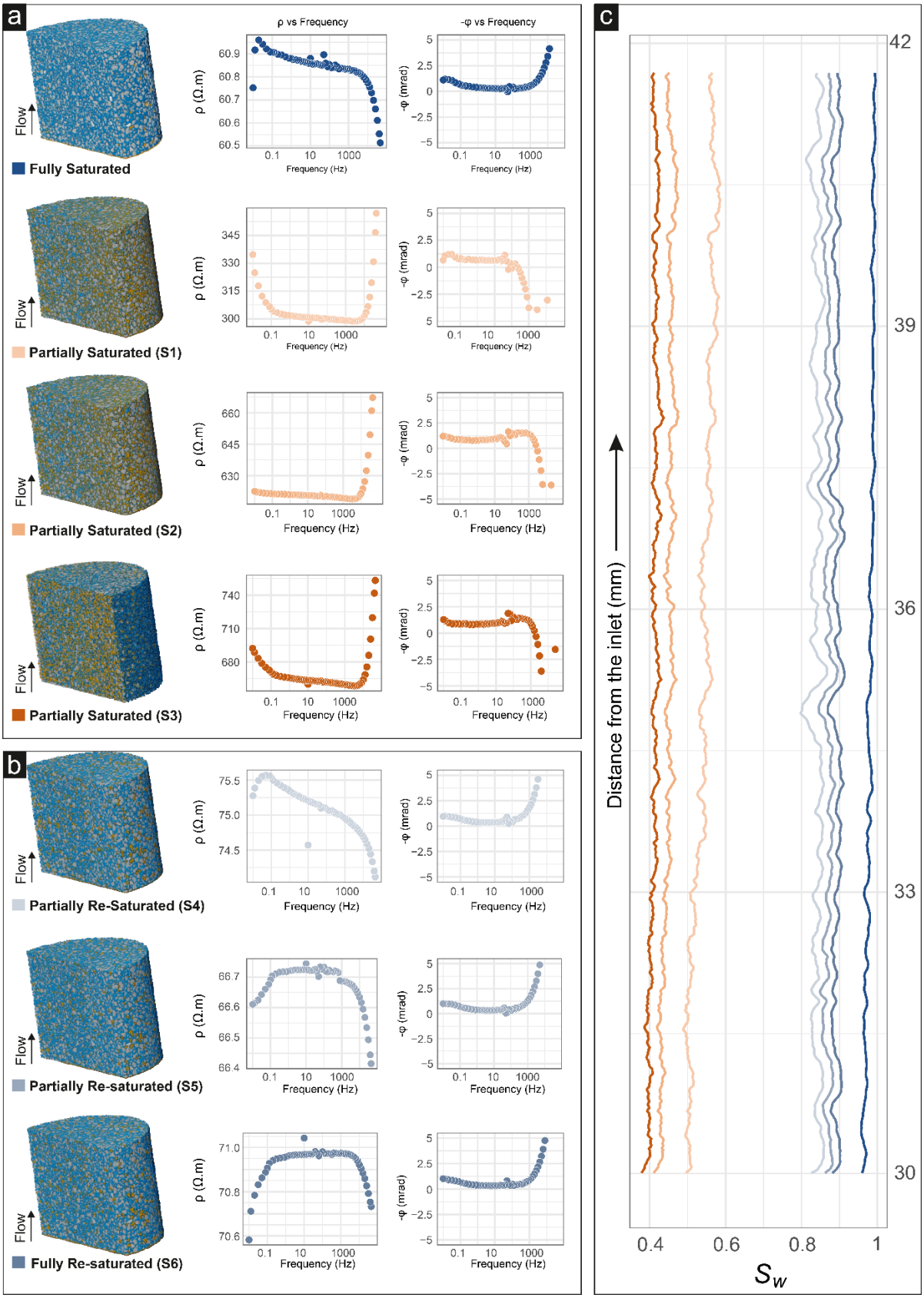

Figure 3. SIP results across different saturation states during (**a**) the drainage- (**b**) imbibition cycle. (**c**) The saturation profiles of each step of the experiment are shown in shading blue and red.

3.2. Effect of water saturation on the saturation exponent

The saturation exponent n in Archie's law reflects how electrical resistivity responds to changes in pore water saturation. Its value depends on fluid connectivity, pore structure, and saturation history, rather than being a fixed property of the material (Glover, 2017). Here, we analyse the variation of n during drainage and imbibition to evaluate how changes in fluid distribution affect the electrical response of the sample. Comparisons with µCT imaging and previous studies provide insight into the pore-scale mechanisms controlling resistivity in partially saturated porous media.

We fitted the saturation exponent n separately for each process, yielding n = 2.77 for drainage and n = 1.12 for imbibition, with a general global fit resulting in n = 2.71 (**Figure 4**a). These contrasted values fall within or close to the range of saturation exponents (from 1.3 to 2.5 in Glover, 2017) reported in the literature for sandstones and unconsolidated sands. The variation in n between drainage and imbibition supports that, contrary to cementation exponent m, the saturation exponent n is not a fixed value for a specific material, but is rather a dynamic parameter responding to changes in the pore-scale fluid distribution, connectivity, and wettability. Glover (2017) emphasized that lower n values (1.3–2.5) are characteristic of imbibition, where water preferentially fills smaller, well-connected pores and re-establishes conductive pathways. In contrast, during drainage, water is displaced from larger pores (**Fig. 6**a and b), increasing tortuosity (**Figure 5**) and decreasing connectivity (Error! Reference source not found.e), which results in higher n values (2.5 – 3), consistent with the µCT images. These observations, supported by theoretical and empirical studies (e.g., Ghanbarian et al. 2013; Berg, 2013; Purcell, 1949), confirm that the saturation exponent is fundamentally influenced by saturation history and the connectivity of the wetting phase. Mustofa et al. (2022)

further demonstrated that even the water injection method can influence n in unconsolidated sands. Injection from the middle produced n = 1.252, attributed to uniform water film distribution, while bottom injection gave a lower n = 1.217 due to more heterogeneous saturation. In our case, bottom injection also yielded n = 2.77 during drainage and n = 1.12 during imbibition, confirming that saturation history, injection strategy, and fluid configuration all affect n.

We extended the analysis beyond n-value fitting by simulating the resistivity index with *PNFlow*, using the static pore network derived from the dry µCT scan. The simulation reproduced general trends in agreement with the measured *RI*, particularly the increase in *RI* during gas invasion (S1–S3) and its decrease upon imbibition (S4–S6), which validate the dominant role of pore connectivity and fluid redistribution in governing bulk resistivity (Blunt et al. 2001). However, systematic deviations at intermediate saturations were observed, with experimental *RI* values exceeding model predictions during drainage and falling below them during imbibition (**Fig 4**b). These observations are consistent with earlier findings on resistivity hysteresis and capillary trapping in porous media (Knight, 1991; Taylor & Barker 2002; Mustofa et al. 2022). Knight (1991) demonstrated that, at equal saturation levels, resistivity during drainage consistently exceeds that observed during imbibition due to differences in fluid redistribution, highlighting hysteresis. Our results echoed this behaviour, with a sharp increase in *RI* at 54% saturation (S3) during drainage, similar to the "resistivity jump" observed by Knight during imbibition.

To further explore this pattern, we evaluated both geometric tortuosity (τ_g) and electrical tortuosity (τ_e) over the same saturation steps. Comparison between τ_e and τ_g revealed good agreement under saturated conditions, but a pronounced divergence at lower saturations (**Fig. 5**). In general, SIP-based estimates of tortuosity (based on Archie's law, eq. 13) are influenced by interfacial polarization, water films, and partial pore occupancy, effects not captured in

geometry-based models (Maineult et al. 2018; Mustofa et al. 2022). The simultaneous μCT–SIP method improves accuracy by directly resolving phase distributions and linking them in real time to electrical responses, making these effects measurable and relevant for petrophysical models.

Table 2. Archie's parameters of the sand sample determined and used in this study

Archie's parameter	**Corresponding value**	**Determination method**
ρ_0	10.365 (Ω.m)	Lab conductivimeter
ρ_f	62.44 (Ω.m)	SIP
ϕ	0.32	μCT
F	6.024	Eq. 5
m	1.67	Eq. 6
n (general fitting)	3.02	Eq. 8 (log-log fitting of S_w vs RI)

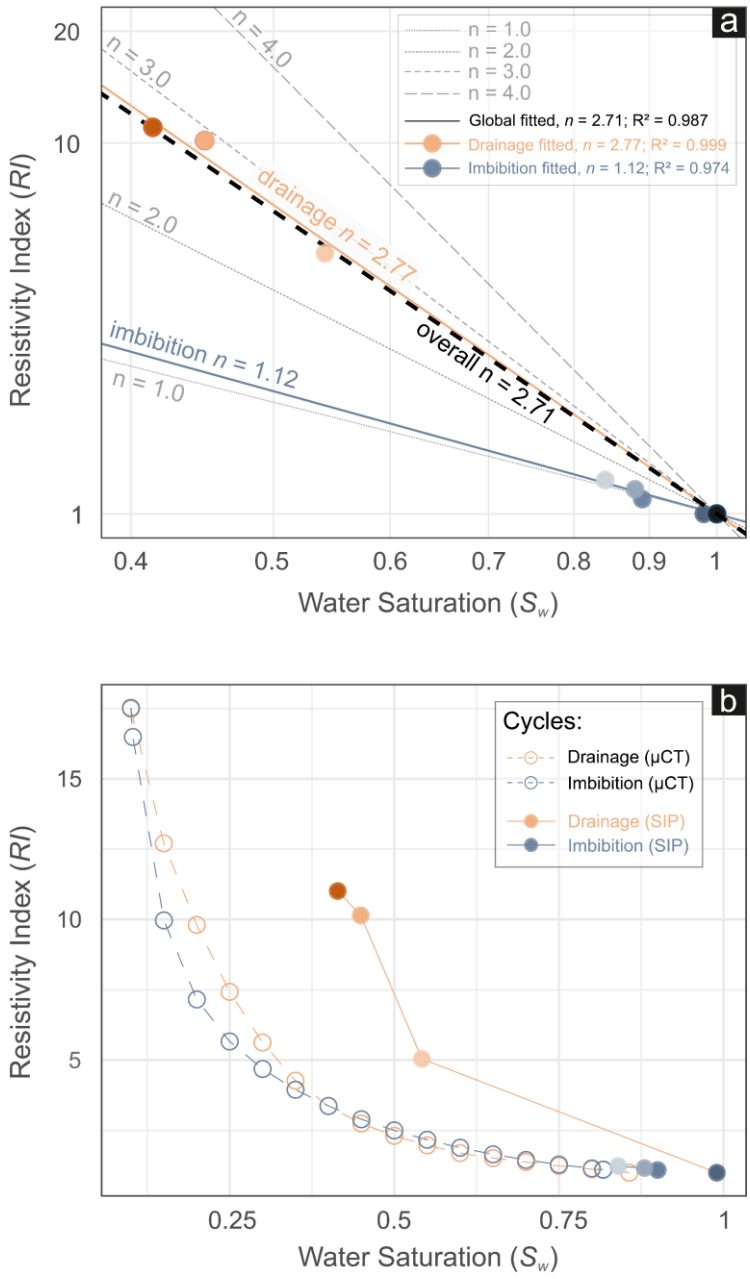

Figure 4. (**a**) **R**esistivity Index (*RI*) versus Water Saturation (S_w) for the studied sample, plotted on a log-log scale. The data are separated into drainage (decreasing S_w) and imbibition (increasing S_w) processes, with fitted Archie saturation exponents (n). Reference lines for n = 1.0, 2.0, 3.0, and 4.0 (grey dashed lines) are provided for comparison. The global fitted n (2.71) reflects the overall trend, while process-specific exponents indicate hysteresis: drainage n = 2.77 (discontinuous water phase at low S_w) and imbibition n = 1.12 (reconnected water films at high S_w). Axes range from 0.4 to 1 for S_w and from 1 to 20 for the *RI*. (**b**) Resistivity index (*RI*) calculated from SIP data and μCT images for the drainage-imbibition cycle described in the method section.

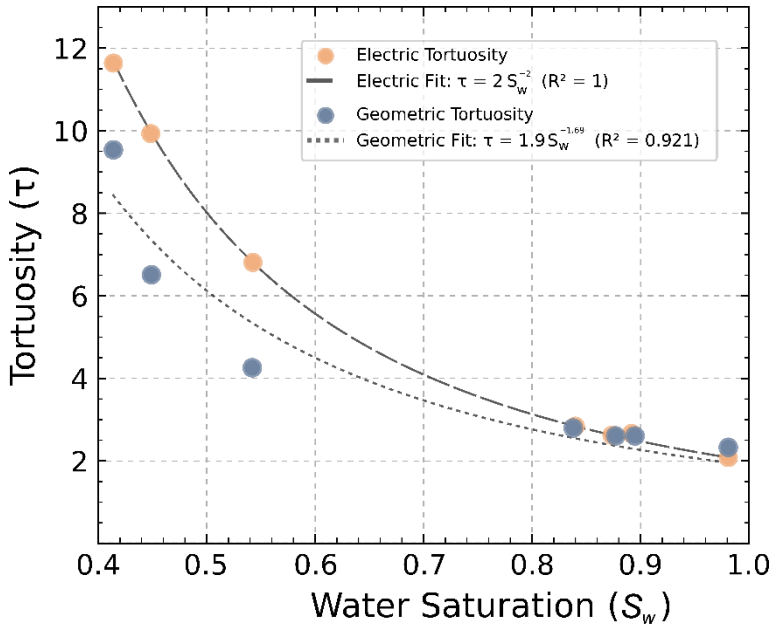

Figure 5. Geometric and electric tortuosity against water saturation (S_w). Both methods shows good agreement at higher saturations while τ_e is obviously higher at lower saturations.

3.3. Linking pore-scale fluid distribution to resistivity: the effect of gas injection on the spatial distribution of the water-phase

A key objective of this study was to explore potential capability of how µCT imaging can inform and refine the interpretation of the joint SIP measurements by linking pore-scale fluid redistribution during drainage and imbibition to macroscopic electrical behaviour. We analysed pore network statistics of water-filled pores and throats across the seven saturation states (**Fig. 6**). Pore network parameters (including pore radius, throat size, and coordination number) of the water-filled pores were extracted and interpreted relative to the dry scan baseline. The pore size distribution of the dry sample (**Fig. S4** and **Table S3**) shows a dominant peak between 40 – 60 µm, with throat radii being predominantly below 30 µm. The coordination number or connectivity (which refers to the number of throats linked to each pore body) ranges from 0 to

over 30, with a modal value between 7 and 8, indicating a connected pore network (Bakke, 2002)

Results from the flow experiment shows that the fluid distribution in the sample varies systematically with varying saturation (**Fig. 6**). During the drainage, water is removed preferentially from larger pores (**Fig. 6** a and Error! Reference source not found.b). The average coordination number of the subnetwork of the water-filled pores declines with decreasing saturation (**Fig. 6**Error! Reference source not found.d), indicating a decrease in water connectivity. Closely associated with this, the tortuosity of the water-filled pore space increases during drainage (**Fig. 5**). For similar gas saturations, localized differences in pore water distribution can cause noticeable change in resistivity and tortuosity, as reported by Knight (1991). Since electrical resistivity is highly sensitive to tortuous current pathways (Fu et al. 2021; Ghanbarian, 2013), the gas injection (reducing pore water connectivity and forcing current through longer, narrower, and more winding channels) leads to a measurable increase in the bulk resistivity of the sample (**Figs 2**a and 4).

Imbibition followed a different trajectory than drainage. Water initially re-entered the sample by preferentially wetting larger pores and throats. **Fig. 6** shows that both throat size and average pore radius of the water-filled pores increase consistently with rising water saturation. Coordination numbers of water-filled pores increased with saturation (**Fig. 6**e and f), indicating the re-establishment of previously disconnected conductive paths. Despite the limited number of observational steps, the implications of these phenomena are reflected in the resistivity index (**Fig. 4**b) and tortuosity (**Fig. 5**) behaviour. The *RI* pattern curve in **Fig. 4**(b) flattens during imbibition, and the saturation exponent (n = 1.12) reflects a smoother reconnection of the water phase. Compared to drainage, where a steep resistivity rise (n = 2.77 in Fig. 4a) marked the breakdown of conductive continuity, imbibition exhibits a more gradual recovery. Tortuosity

trends in **Fig. 5** also support this behaviour, showing decreasing values with increasing saturation, as more direct and less convoluted flow paths reform during wetting.

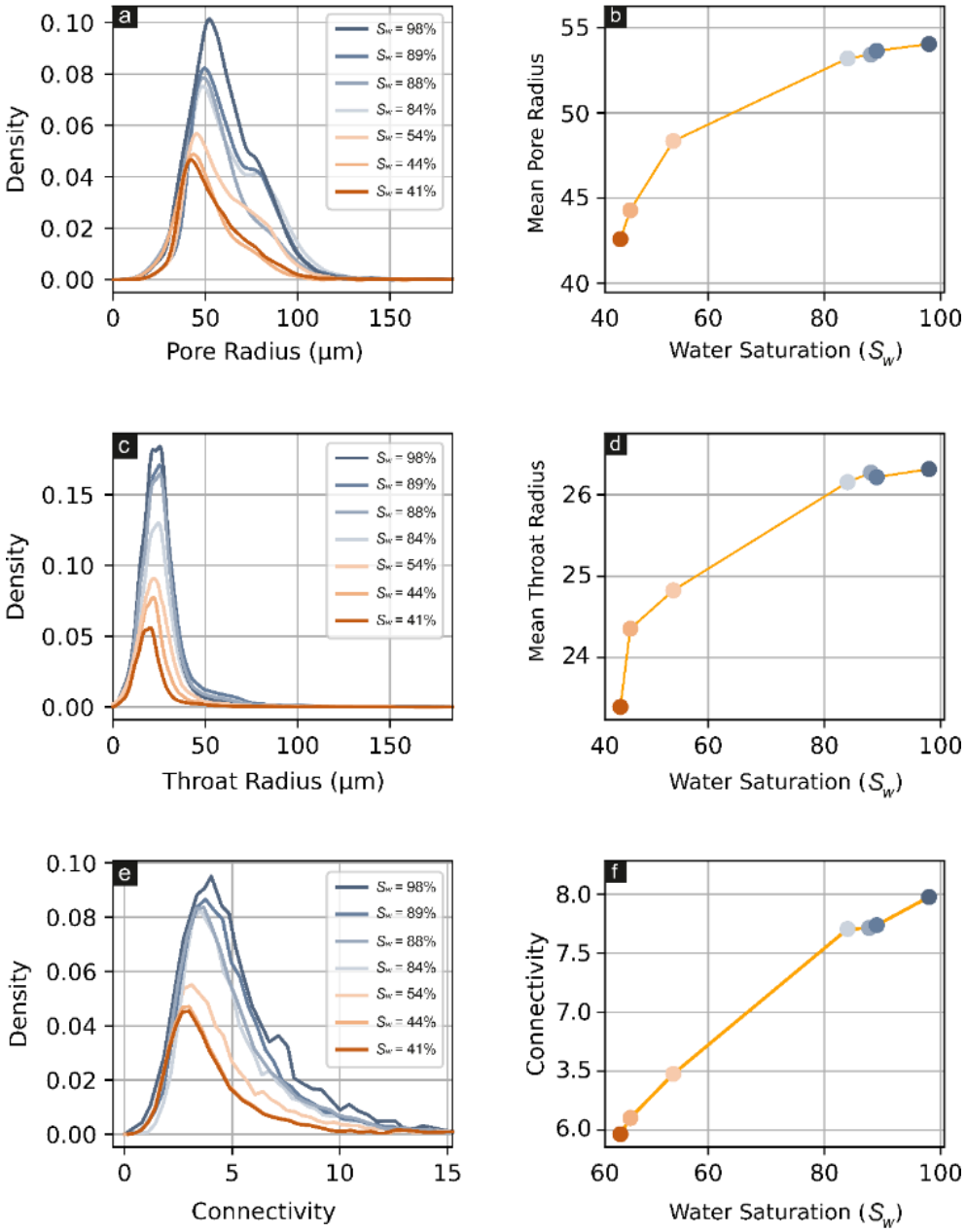

Figure 6. Evolution of pore network statistics of the water-filled pore network for the different saturation steps (S1 – S7) during drainage and imbibition. (**a**) Pore size distribution and (**b**) corresponding average pore radius as a function of water saturation. (**c**) Throat radius distribution and (**d**) corresponding average throat radius versus saturation. (**e**) Coordination number (connectivity) distribution and (**f**) corresponding average coordination number as a function of water saturation.

4. CONCLUSION

This study introduced a combined experimental setup for simultaneous SIP and μCT, designed to explore how fluid saturation affects petrophysical properties in porous media. The aim was not only to measure changes in electrical behaviour but also to visualize changes in fluid distribution simultaneously. The setup provided reliable results under partially saturated conditions and allowed for synchronized acquisition of electrical and structural data, which is an essential step toward interpretations of geophysical signals based on pore-scale observations and process-based petrophysical relationships. The simultaneous μCT and SIP measurements enable a more direct and time-resolved link between spatial distribution of fluids and electrical response, revealing subtle pore-scale effects (such as residual gas disrupting water connectivity or fine-scale heterogeneities driving phase trapping) that contribute to the nonlinearity of resistivity trends.

The combined dataset gave a clearer picture of how gas injection reduces water connectivity and increases the tortuosity of electrical flow paths. μCT images revealed changes in pore occupancy, throat constrictions, and phase trapping, all of which shaped the saturation-resistivity relationship captured by SIP. Saturation exponents derived from electrical data varied significantly between drainage and imbibition, confirming that n is not a fixed property but reflects the underlying fluid configuration. Rather than treating deviations in n as model uncertainty, we interpret them here as signatures of underlying structural and hydraulic complexities, (including, but not limited to, including gas trapping, pore-scale disconnection, and variations in fluid occupancy) which our combined method helps to resolve explicitly. These observations were in line with previous research, but the added value of the approach here lies in its ability to directly visualize what those resistivity trends imply about pore-scale structure and phase connectivity.

Resistivity index simulations based on pore network modelling captured the broad behaviour seen in the data, but fell short in matching experimental results across all saturation levels. This difference pointed to the role of subtle pore-scale features that are hard to capture using simplified models. The study also compared electrical and geometric tortuosity estimates, showing that while both respond to saturation changes, they diverge when the conductive phase becomes disconnected. These discrepancies are informative: they suggest where models need refinement and where assumptions about phase continuity may break down.

Looking ahead, the ability to resolve spatial patterns of fluid occupancy in tandem with electrical properties paves a path toward refining petrophysical models. Incorporating this level of detail can help constrain parameters like the saturation exponent based on physically interpretable processes, rather than using them solely as empirical fits. Ultimately, this combined method improves model validation, guides the development of more predictive formulations, and supports the broader goal of linking geoelectrical measurements to pore-scale physics in complex geological materials. While this study focused on a relatively simple, clean sand that exhibits limited polarization, the experimental setup allows investigating more complex samples and processes where polarization plays an important role. Future work could explore reactive transport or biogeochemical processes known to generate stronger polarization signals, such as clay-rich soils, precipitation of conductive minerals, or microbial activity, where the combined SIP–μCT method could help resolve mechanisms that remain poorly understood.

REFERENCES

Adebayo, Abdulrauf R., Mohamed E. Kandil, Taha M. Okasha, and Modiu L. Sanni. 2017. "Measurements of Electrical Resistivity, NMR Pore Size and Distribution, and x-Ray CT-

Scan for Performance Evaluation of CO2 Injection in Carbonate Rocks: A Pilot Study." *International Journal of Greenhouse Gas Control* 63(October 2016): 1–11. doi:10.1016/j.ijggc.2017.04.016.

Aggelopoulos, C., Klepetsanis, P., Theodoropoulou, M.A., Pomoni, K., Tsakiroglou, C.D., 2005. Large-scale effects on resistivity index of porous media. J. Contam. Hydrol. 77 (4), 299–323. https://doi.org/10.1016/j.jconhyd.2005.02.002.

Allen, P. A., & Allen, J. R., 2013. *Basin analysis: Principles and application to petroleum play assessment*. John Wiley & Sons.

Archie, G. E., 1942. The electrical resistivity log as an aid in determining some reservoir characteristics. *Transactions of the AIME*, *146*(01), 54-62.

Armstrong, Ryan T., Mark L. Porter, and Dorthe Wildenschild. 2012. "Linking Pore-Scale Interfacial Curvature to Column-Scale Capillary Pressure." *Advances in Water Resources* 46: 55–62. doi:10.1016/j.advwatres.2012.05.009.

Atekwana, Estella A., and Lee D. Slater., 2009. "Biogeophysics: A New Frontier in Earth Science Research." *Reviews of Geophysics* 47(4): 1–30. doi:10.1029/2009rg000285.

Bakke, Stig., 2002. "Process Based Reconstruction of Sandstones and Prediction of Transport Properties." (i): 311–43.

Bauer, D., S. Youssef, M. Han, S. Bekri, E. Rosenberg, M. Fleury, & O. Vizika., 2011. "From Computed Microtomography Images to Resistivity Index Calculations of Heterogeneous Carbonates Using a Dual-Porosity Pore-Network Approach: Influence of Percolation on the Electrical Transport Properties." *Physical Review E - Statistical, Nonlinear, and Soft Matter Physics* 84(1): 1–12. doi:10.1103/PhysRevE.84.011133.

Berg, Steffen, Holger Ott, Stephan A. Klapp, Alex Schwing, Rob Neiteler, Niels Brussee, Axel

Makurat, et al. 2013. “Real-Time 3D Imaging of Haines Jumps in Porous Media Flow.” *Proceedings of the National Academy of Sciences of the United States of America* 110(10): 3755–59. doi:10.1073/pnas.1221373110.

Berkowitz, B., & Scher, H. (1998). Theory of anomalous chemical transport in random fracture networks. *Physical Review E*, *57*(5), 5858.

Binley, Andrew, Giorgio Cassiani, Roy Middleton, and Peter Winship. 2002. “Vadose Zone Flow Model Parameterisation Using Cross-Borehole Radar and Resistivity Imaging.” *Journal of Hydrology* 267(3–4): 147–59. doi:10.1016/S0022-1694(02)00146-4.

Binley, Andrew, and Andreas Kemna. 2005. Hydrogeophysics *DC Resistivity and Induced Polarization Methods*. doi:10.1007/1-4020-3102-5_5.

Blunt, M. J. (2001). Flow in porous media—pore-network models and multiphase flow. *Current opinion in colloid & interface science*, *6*(3), 197-207.

Bultreys, Tom, Wesley De Boever, and Veerle Cnudde. 2016. “Imaging and Image-Based Fluid Transport Modeling at the Pore Scale in Geological Materials: A Practical Introduction to the Current State-of-the-Art.” *Earth-Science Reviews* 155: 93–128. doi:10.1016/j.earscirev.2016.02.001.

Carothers, J. E.: A statistical study of the formation factor relation, Log Anal., 9, 13–20, 1968.

Cimpoiaşu, Mihai O., Oliver Kuras, Paul B. Wilkinson, Tony Pridmore, & Sacha J. Mooney., 2021. “Hydrodynamic Characterization of Soil Compaction Using Integrated Electrical Resistivity and X-Ray Computed Tomography.” *Vadose Zone Journal* 20(4): 1–15. doi:10.1002/vzj2.20109.

Clennell, M.B. 1997. Tortuosity: A guide through the maze. In: M.A. Lovell and P.K. Harvey, editors, Developments in petrophysics. Geol. Soc., London. p. 299–344.

Coleman, S.W., J.C. Vassilicos., 2008. Transport properties of saturated and unsaturated porous fractal materials. Phys. Rev. Lett. 100:035504. doi:10.1103/PhysRevLett.100.035504

Cong-Thi, D., Dieu, L. P., Caterina, D., De Pauw, X., Thi, H. D., Ho, H. H., et al., 2024. Quantifying salinity in heterogeneous coastal aquifers through ERT and IP: Insights from laboratory and field investigations. *Journal of Contaminant Hydrology*, *262*, 104322. https://doi.org/10.1016/j.jconhyd.2024.104322.

Dimech, A., Cheng, L., Chouteau, M., Chambers, J., Uhlemann, S., Wilkinson, P., et al., 2022. A Review on Applications of Time-Lapse Electrical Resistivity Tomography Over the Last 30 Years : Perspectives for Mining Waste Monitoring. Surveys in Geophysics, 43(6), 1699–1759.

Doussan, Claude, and Stéphane Ruy., 2009. "Prediction of Unsaturated Soil Hydraulic Conductivity with Electrical Conductivity." *Water Resources Research* 45(10): 1–12. doi:10.1029/2008WR007309.

Dullien, F.A.L., 1979. Porous media: Fluid transport and pore structure. Academic Press, San Diego.

Epstein, N., 1989. On tortuosity and the tortuosity factor in flow and diffusion through porous media. Chem. Eng. Sci. 44:777–779. doi:10.1016/0009-2509(89)85053-5

Fu, Jinlong, Hywel R. Thomas, and Chenfeng Li., 2021. "Tortuosity of Porous Media: Image Analysis and Physical Simulation." *Earth-Science Reviews* 212(November 2020): 103439. doi:10.1016/j.earscirev.2020.103439.

Garba, M.A., Vialle, S., Madadi, M., Gurevich, B., Lebedev, M., 2019. Electrical formation factor of clean sand from laboratory measurements and digital rock physics. Solid Earth 10 (5), 1505–1517. https://doi.org/10.5194/se-10-1505-2019.

Ghanbarian, Behzad, Allen G. Hunt, Robert P. Ewing, & Muhammad Sahimi., 2013. "Tortuosity in Porous Media: A Critical Review." *Soil Science Society of America Journal* 77(5): 1461–77. doi:10.2136/sssaj2012.0435.

Glover, P. W., 2017. A new theoretical interpretation of Archie's saturation exponent. Solid Earth, 8(4), 805-816.

Glover, P. W., 2016. Archie's law–a reappraisal. *Solid Earth*, *7*(4), 1157-1169.

Glover, P. W. J., 2015. *Geophysical properties of the near surface Earth: electrical properties, Treatise on Geophysics, 11, 89–137*.

Glover, P. W. J., 2009. What is the cementation exponent? A new interpretation. *The Leading Edge*, *28*(1), 82-85.

Glover, P. W., Hole, M. J., & Pous, J., 2000. A modified Archie's law for two conducting phases. *Earth and Planetary Science Letters*, *180*(3-4), 369-383.

Rivero, O. G., 1977, June. Some considerations about the possible use of the parameters a and m as a formation evaluation tool through well logs. In *SPWLA Annual Logging Symposium* (pp. SPWLA-1977). SPWLA.

Hao, Na, Jianshe Ye, Li Zhao, Meng Sun, Yuqing You, Chi Zhang, Junnan Cao, et al., 2021. "Evaluating Iron Remediation with Limestone Using Spectral Induced Polarization and Microscopic Techniques." *Science of the Total Environment* 800: 149641. doi:10.1016/j.scitotenv.2021.149641.

Jougnot, D., Ghorbani, A., Revil, A., Leroy, P., & Cosenza, P., 2010. Spectral induced polarization of partially saturated clay-rocks: A mechanistic approach. *Geophysical Journal International*, *180*(1), 210-224.

Hermans, Thomas, Goderniaux, P., Jougnot, D., Fleckenstein, J. H., Brunner, P., Nguyen, F., et al., 2023. Advancing measurements and representations of subsurface heterogeneity and dynamic processes: towards 4D hydrogeology. Hydrology and Earth System Sciences, 27(1), 255–287. https://doi.org/10.5194/hess-27-255-2023

Izumoto, Satoshi, Johan Alexander Huisman, Egon Zimmermann, Joris Heyman, Francesco Gomez, Hervé Tabuteau, Romain Laniel, et al., 2022. "Pore-Scale Mechanisms for Spectral Induced Polarization of Calcite Precipitation Inferred from Geo-Electrical Millifluidics." *Environmental Science and Technology* 56(8): 4998–5008. doi:10.1021/acs.est.1c07742.

Johansson, Sara, Matteo Rossi, Stephen A. Hall, Charlotte Sparrenbom, David Hagerberg, Erika Tudisco, Håkan Rosqvist, & Torleif Dahlin., 2019. "Combining Spectral Induced Polarization with X-Ray Tomography to Investigate the Importance of DNAPL Geometry in Sand Samples." *Geophysics* 84(3): E173–88. doi:10.1190/geo2018-0108.1.

Knight, R., 1991, Hysteresis in the electrical resistivity of partially saturated sandstones, Geophysics, 56(12), 2139-2147, doi:10.1190/1.1443028.

Leroy, P., A. Revil, A. Kemna, P. Cosenza, and A. Ghorbani., 2008. "Complex Conductivity of Water-Saturated Packs of Glass Beads." *Journal of Colloid and Interface Science* 321(1): 103–17. doi:10.1016/j.jcis.2007.12.031.

Lesmes, David P., and Kevin M. Frye., 2001. "Influence of Pore Fluid Chemistry on the Complex Conductivity and Induced Polarization Responses of Berea Sandstone." *Journal of Geophysical Research: Solid Earth* 106(B3): 4079–90. doi:10.1029/2000jb900392.

Ma, Xinmin, Nimrod Schwartz, Chen Chao, Jing Li, Teng Xia, Alex Furman, and Deqiang Mao., 2025. "Unveiling Spectral Induced Polarization Responses of ZVI-AC-Sand Mixtures in Groundwater Remediation." *Journal of Geophysical Research: Solid Earth*

130(3): 1–19. doi:10.1029/2024JB030107.

Maineult, A., D. Jougnot, and A. Revil., 2018, Variations of petrophysical properties and spectral induced polarization in response to drainage and imbibition: a study on a correlated random tube network, *Geophys. J. Int.*, *212*(2), 1398-1411, doi:10.1093/gji/ggx474.

Matyka, M., A. Khalili, and Z. Koza., 2008. Tortuosity–porosity relation in porous media flow. Phys. Rev. E 78:026306. doi:10.1103/Phys Rev E.78.026306

Mawer, C., R. Knight, P. K. Kitanidis., 2015. Relating relative hydraulic and electrical conductivity in the unsaturated zone, Water Resour. Res., 51(1), 599-618, doi:10.1002/2014wr015658.

Moldrup, P., T. Olesen, T. Komatsu, P. Schjonning, and D.E. Rolston., 2001. Tortuosity, diffusivity, and permeability in the soil liquid and gaseous phases. Soil Sci. Soc. Am. J. 65:613–623. doi:10.2136/sssaj2001.653613x

Morrow, N. R., Chatzis, I., & Taber, J. J., 1988. Entrapment and mobilization of residual oil in bead packs. *SPE Reservoir Engineering*, *3*(03), 927-934.

Mustofa, M. B., U. Fauzi, F. D. E. Latief, and W. Warsa., 2022, Experimental and modeling of electrical resistivity changes due to micro-spatial distribution of fluid for unconsolidated sand, *J. Pet. Sci. Eng.*, *208*, 109472, doi:10.1016/j.petrol.2021.109472.

Norbisrath, J. H., Eberli, G. P., Laurich, B., Desbois, G., Weger, R. J., & Urai, J. L., 2015. Electrical and fluid flow properties of carbonate microporosity types from multiscale digital image analysis and mercury injection. *AAPG bulletin*, *99*(11), 2077-2098.

Pentland, Christopher H., Rehab El-Maghraby, Stefan Iglauer, and Martin J. Blunt., 2011. "Measurements of the Capillary Trapping of Super-Critical Carbon Dioxide in Berea

Sandstone." *Geophysical Research Letters* 38(6): 2007–10. doi:10.1029/2011GL046683.

Porter, C. R., & Carothers, J. E., 1970, May. Formation factor-porosity relation derived from well log data. In *SPWLA Annual Logging Symposium* (pp. SPWLA-1970). SPWLA.

Purcell, W. R., 1949. Capillary pressures-their measurement using mercury and the calculation of permeability therefrom. *Journal of Petroleum Technology*, *1*(02), 39-48

Raeini, A. Q., Bijeljic, B., & Blunt, M. J., 2018. Generalized network modeling of capillary-dominated two-phase flow. *Physical Review E*, *97*(2), 023308.

Rembert, F., Stolz, A., Soulaine, C., & Roman, S., 2023. A microfluidic chip for geoelectrical monitoring of critical zone processes. *Lab on a Chip*, *23*(15), 3433-3442.

Rembert, F., Léger, M., Jougnot, D., & Luquot, L., 2023. Geoelectrical and hydro-chemical monitoring of karst formation at the laboratory scale. *Hydrology and Earth System Sciences*, *27*(2), 417-430.

Revil, A., Schmutz, M., & Batzle, M. L., 2011. Influence of oil wettability upon spectral induced polarization of oil-bearing sands. *Geophysics*, *76*(5), A31-A36.

Revil, A., and N. Florsch., 2010. "Determination of Permeability from Spectral Induced Polarization in Granular Media." *Geophysical Journal International* 181(3): 1480–98. doi:10.1111/j.1365-246X.2010.04573.x.

Revil, A., Kessouri, P., & Torres-Verdín, C., 2014. Electrical conductivity, induced polarization, and permeability of the Fontainebleau sandstone. *Geophysics*, *79*(5), D301-D318.

Sahimi, M., 1993. Flow phenomena in rocks: From continuum models to fractals, percolation, cellular automata, and simulated annealing. *Rev. Mod. Phys.* 65:1393–1534. doi:10.1103/RevModPhys.65.1393.

Scheidegger, A.E. 1974. The physics of flow through porous media. 3rd ed. Univ. of Toronto Press, Toronto.

Schmutz, M., A. Revil, P. Vaudelet, M. Batzle, P. Femenía Viñao, and D. D. Werkema., 2010. "Influence of Oil Saturation upon Spectral Induced Polarization of Oil-Bearing Sands." *Geophysical Journal International* 183(1): 211–24. doi:10.1111/j.1365-246X.2010.04751.x.

Schopper, J.R. 1966. A theoretical investigation on the formation factor/permeability/porosity relationship using a network model. *Geophys. Prospect.* 14:301–341. doi:10.1111/j.1365-2478.1966.tb01763.x

Singha, K., Day-Lewis, F. D., Johnson, T., & Slater, L. D., 2015. Advances in interpretation of subsurface processes with time-lapse electrical imaging. *Hydrological Processes*, *29*(6), 1549-1576.

Slater L, Binley. A., 2021. Advancing hydrological process understanding from long-term resistivity monitoring systems. WIREs Water 8(3), e1513.

Taylor, S., Barker, R., 2002. Resistivity of partially saturated triassic sandstone. Geophys. Prospect. 50 (6), 603–613. https://doi.org/10.1046/j.1365-2478.2002.00339.x

Timur, A., Hempkins, W. B., & Worthington, A. E., 1972, May. Porosity and pressure dependence of formation resistivity factor for sandstones. In *Trans CWLS 4th Formation Evaluation Symp* (Vol. 30).

Tokunaga, Tetsu K., 2009. "Hydraulic Properties of Adsorbed Water Films in Unsaturated Porous Media." *Water Resources Research* 45(6): 1–9. doi:10.1029/2009WR007734.

Tye, F.L., 1983. Tortuosity. J. Power Sources 9:89–100. doi:10.1016/0378-7753(83)80026-3

Umezawa, R., M. Katsura, and S. Nakashima., 2021. Effect of water saturation on the electrical conductivity of microporous silica glass, *Transp. Porous Media*, *138*(1), 225-243, doi:10.1007/s11242-021-01601-6.

Weller, A., Breede, K., Slater, L., & Nordsiek, S., 2011. Effect of changing water salinity on complex conductivity spectra of sandstones. *Geophysics*, *76*(5), F315-F327.

Weller, A., Slater, L., Binley, A., Nordsiek, S., & Xu, S., 2015. Permeability prediction based on induced polarization: Insights from measurements on sandstone and unconsolidated samples spanning a wide permeability range. *Geophysics*, *80*(2), D161-D173.

Wildenschild, Dorthe, and Adrian P. Sheppard., 2013. "X-Ray Imaging and Analysis Techniques for Quantifying Pore-Scale Structure and Processes in Subsurface Porous Medium Systems." *Advances in Water Resources* 51: 217–46. doi:10.1016/j.advwatres.2012.07.018.

Wyllie, M.R.J. 1957. The fundamentals of electric log interpretation. Academic Press, New York.

Yan, Weichao, Jianmeng Sun, Jinyan Zhang, Weiguo Yuan, Li Zhang, Likai Cui, and Huaimin Dong. 2018. "Studies of Electrical Properties of Low-Resistivity Sandstones Based on Digital Rock Technology." *Journal of Geophysics and Engineering* 15(1): 153–63. doi:10.1088/1742-2140/aa8715.

Zhang, Zeyu, Sabine Kruschwitz, Andreas Weller, and Matthias Halisch. 2018. "Enhanced Pore Space Analysis by Use of μ-CT, MIP, NMR, and SIP." *Solid Earth* 9(6): 1225–38. doi:10.5194/se-9-1225-2018.

Zhang, Z., Liu, L., Li, C., Cai, J., Ning, F., Meng, Q., & Liu, C., 2021. Fractal analyses on saturation exponent in Archie's law for electrical properties of hydrate-bearing porous media. *Journal of Petroleum Science and Engineering*, *196*, 107642.

Zimmermann, E., and J. A. Huisman. 2024. "The Effect of Heterogeneous Contact Impedances on Complex Resistivity Measurements." *Geophysical Journal International* 236(3): 1234–45. doi:10.1093/gji/ggad477.

Zimmermann, E., A. Kemna, J. Berwix, W. Glaas, H. M. Münch, and J. A. Huisman., 2008. "A High-Accuracy Impedance Spectrometer for Measuring Sediments with Low Polarizability." *Measurement Science and Technology* 19(10). doi:10.1088/0957-0233/19/10/105603.